

## Electron density images of the middle- and high-latitude magnetosphere in response to the solar wind

Jiannan Tu,<sup>1</sup> Paul Song,<sup>1</sup> Bodo W. Reinisch,<sup>1</sup> Xueqin Huang,<sup>1</sup> James L. Green,<sup>2</sup> Harald U. Frey,<sup>3</sup> and Patricia H. Reiff<sup>4</sup>

Received 20 July 2005; revised 31 August 2005; accepted 5 October 2005; published 15 December 2005.

[1] Electron density distributions and plasma dynamics in the middle- and high-latitude dayside magnetosphere are studied with observations from the IMAGE radio plasma imager. Remote measurements of the electron densities along magnetic field lines were made before and during a magnetic storm when the solar wind and interplanetary magnetic field (IMF) impinging on the magnetopause varied considerably. Several regions of different density distribution characteristics, including plasmasphere, plasma trough, subauroral/auroral density depletion, density enhancements in the aurora/cusp, and polar cap, are identified in “two-dimensional images,” i.e., along the satellite orbit and field lines. The plasma dynamics, such as the plasma refilling in the outer plasmasphere and the plasma acceleration in the aurora/cusp region, are inferred from density gradients along the field lines. It is shown that the densities and locations of the plasma regions vary in accordance with the solar wind, particularly with the IMF variations for the case examined. In the partial recovery phase of the magnetic storm when the IMF was northward, the density depletion region expanded to wider latitude range and extended to lower altitudes, with much lower densities than those in the density depletion regions of the other RPI measurement periods. The density enhancements associated with the aurora/cusp region were not visible, possibly because of the diffusive nature of the dayside aurora and higher-latitude location of the cusp during this period. At the peak of the storm, characterized by a persistent southward IMF  $B_z$ , all plasma regions moved to lower  $L$  shells. The results imply that the solar wind/IMF effects should be included in any statistical study of the electron density distributions in these regions.

**Citation:** Tu, J., P. Song, B. W. Reinisch, X. Huang, J. L. Green, H. U. Frey, and P. H. Reiff (2005), Electron density images of the middle- and high-latitude magnetosphere in response to the solar wind, *J. Geophys. Res.*, 110, A12210, doi:10.1029/2005JA011328.

### 1. Introduction

[2] The plasma density distributions in the Earth's magnetosphere are primarily determined by the plasma transport as well as the plasma sources (solar wind and ionosphere). One of fundamental factors that influences the plasma transport is the solar wind/magnetosphere interaction. The plasmapause location and the plasma density distributions beyond the plasmapause are sensitive to variations of the solar wind and interplanetary magnetic field (IMF) because of the magnetospheric convection produced by the solar wind/magnetosphere interactions. In order to better under-

stand the magnetospheric electron plasma distributions, it is important to examine their dynamical relationship with the solar wind. This can best be accomplished from remotely imaging large regions of electron densities in the middle- to high-latitude magnetosphere in which the location of open and closed field lines can change rapidly.

[3] The density distributions in the plasmasphere have been extensively studied and the responses of the plasmasphere and its boundary, the plasmapause, to the solar wind/IMF variations, in terms of geomagnetic activities, have been documented in numerous publications [e.g., *Lemaire and Gringauz*, 1998, and references therein]. Nevertheless, the plasma density distributions in the plasma trough, auroral zone, cusp, and polar cap, as well as their variations as functions of magnetospheric and upstream solar wind conditions, are not well understood. The empirical relation of the equatorial density as function of  $L$  value and magnetic local time (MLT) presented by *Carpenter and Anderson* [1992] has been often cited in connection with the densities in the plasma trough. Several similar empirical relations have been developed in recent years for the equatorial electron densities [*Gallagher et al.*, 2000; *Goldstein et al.*,

<sup>1</sup>Center for Atmospheric Research, University of Massachusetts-Lowell, Lowell, Massachusetts, USA.

<sup>2</sup>NASA Goddard Space Flight Center, Greenbelt, Maryland, USA.

<sup>3</sup>Space Sciences Laboratory, University of California, Berkeley, Berkeley, California, USA.

<sup>4</sup>Department of Physics and Astronomy, Rice University, Houston, Texas, USA.

2001; *Sheeley et al.*, 2001; *Denton et al.*, 2002, 2004]. Using a large data set from the Polar spacecraft plasma wave measurements, *Denton et al.* [2002] found that the latitudinal dependence of both the plasmaspheric and plasma trough density could be represented by a power law form with a single formula for the power law index. Their latitudinal dependence of the densities is quite similar to that derived from the active remote sounding by *Reinisch et al.* [2004] and *Huang et al.* [2004] for plasmaspheric densities. However, the dependence of the plasma trough densities on the solar wind/IMF conditions has not been explicitly addressed until now.

[4] Electron densities at high latitudes have been sampled using in situ measurement techniques for decades but instantaneous measurements of spatially extended regions by radio sounding were not possible until recently. *Persoon et al.* [1983] developed a statistical empirical model of electron densities in the polar cap for the radial distance range of 2.1–4.66  $R_E$ . They found that the radial distance dependence of the electron density followed a power law with an exponent of  $-3.85$ , implying an outward flow velocity of ions increasing linearly with radial distance. *Chandler et al.* [1991] studied ion densities for  $O^+$ ,  $H^+$ , and  $He^+$  in the altitude range of 1000–4000 km measured by the retarding ion mass spectrometer on the DE-1 satellite. Their results illustrated that  $O^+$  is the dominant ion species up to 4000 km altitude in the polar cap. *Johnson et al.* [2001] presented maps of thermal electron densities in the auroral zone and polar cap at  $\sim 1 R_E$  altitude, covering all magnetic local time. The density variations associated with solar illumination and hence the ionospheric ionization rate variations, along with the auroral density cavities, are clearly seen in those maps. *Johnson and Wygant* [2003] further showed that the effects of the solar illumination on the polar cap densities extend up to 3.5  $R_E$  in altitude. *Laakso and Grard* [2002] studied the statistical distributions of the electron densities in the auroral zone and polar cap in the radial distance range of 2–9  $R_E$ . Their results demonstrated that the electron densities at high latitudes increase at all distances with increasing geomagnetic activity, with larger increases during local summer than during local winter. They also showed examples of enhanced polar cap densities in response to the sudden storm commencements (SSC).

[5] Recently, the radio plasma imager (RPI) [*Reinisch et al.*, 2000] on the IMAGE satellite [*Burch et al.*, 2001] has provided nearly instantaneous measurements of the electron density distribution along a magnetic field line [*Reinisch et al.*, 2001]. Such measurements were used to study the dependence of the polar cap electron densities on the radial distance and geomagnetic activity [*Nsumei et al.*, 2003] to a high degree of accuracy on a timescale never before accomplished. Their study established a quantitative relation between the polar cap electron densities and the geomagnetic activity, in the radial distance range of 1.4 to 5  $R_E$ .

[6] In this study we take advantage of the radio sounding technique implemented by IMAGE/RPI to combine multiple (nearly instantaneous) measurements of the field-aligned electron density profiles to derive two-dimensional electron density images from the IMAGE orbit down to altitude of  $\sim 3000$  km. Such density images allow us, for the first time, to examine the various plasma regions (plasmasphere, plasma trough, aurora/cusp and polar cap) in “two dimen-

sions,” i.e., along the satellite orbit and the magnetic field lines. We show that the plasma densities in these regions and the location of these plasma regions vary in accordance with the solar wind, particularly IMF variations for the case studied. The observations suggest that the solar wind/IMF effects should be taken into account when interpreting statistically averaged electron density distributions in the magnetosphere.

## 2. Measurement and Density Inversion Technique

[7] The radio plasma imager (RPI) [*Reinisch et al.*, 2000] on the IMAGE satellite, in active sounding modes, transmits coded signals with frequencies sweeping from 3 kHz to 3 MHz and listens to the echoes. The received signals are plotted in the form of plasmagrams, a color-coded display of signal amplitude as function of frequency and echo delay time. Echoes that experience the same dispersion during the propagation form a distinct trace in the plasmagram. Under certain conditions [see *Reinisch et al.*, 2001; *Fung and Green*, 2005] the traces represent the reflected signals that propagated along a magnetic field line from the satellite. Natural waves are received in a passive observation mode and are displayed as a dynamic spectrum [*Reinisch et al.*, 2000; *Green et al.*, 2000, 2004].

[8] By scaling the traces in a plasmagram and using the density inversion algorithm based on the ionospheric density inversion technique of *Huang and Reinisch* [1982], we can derive a density distribution along a field line almost instantaneously [*Huang et al.*, 2004]. For the case studied here, the duration for obtaining a trace is less than 46 s and the typical duration is about 20 s. Figure 1 displays a plasmagram obtained by the RPI at 1845:49 UT on 16 April 2002, with measurement duration of  $\sim 40$  s. There is a trace extending from  $\sim 111$  kHz to  $\sim 819$  kHz and a virtual range to  $\sim 1.4 R_E$  (the virtual range is the echo delay time multiplied by one half of the vacuum speed of light). The local (at the satellite location) electron plasma, electron cyclotron, and upper hybrid resonances are seen as vertical lines of enhanced signals. With the scaled trace (the thin curve on the trace), the electron density along the field line is calculated using the inversion algorithm described by *Huang et al.* [2004], as shown in Figure 2. The density at 1.4  $R_E$  radial distance is  $\sim 3200 \text{ cm}^{-3}$  and decreases along the field line to  $\sim 35 \text{ cm}^{-3}$  at 2.6  $R_E$  where the satellite was located. The typical uncertainty of the derived electron densities due to the uncertainty of determining frequencies along the echoes is less than 6%. The radial distance resolution of the derived electron density profiles depends on the altitude: At altitudes of 3–4  $R_E$  it is up to 0.075  $R_E$  (about 480 km); at altitude of about 3000 km, it can be as good as 0.003  $R_E$  (about 20 km). When the satellite flies across an extended region, a sequence of such density profiles is obtained and a “two-dimensional” density image along the satellite orbit and the magnetic field lines can be constructed. Although the measurement of each individual field-aligned density profile is nearly instantaneous, each density image consists of multiple field-aligned density profiles along an orbit segment of about 1 hour duration. Therefore the density images derived from multiple field-aligned density profiles may not be purely spatial structures. Nevertheless, they provide useful information regarding the

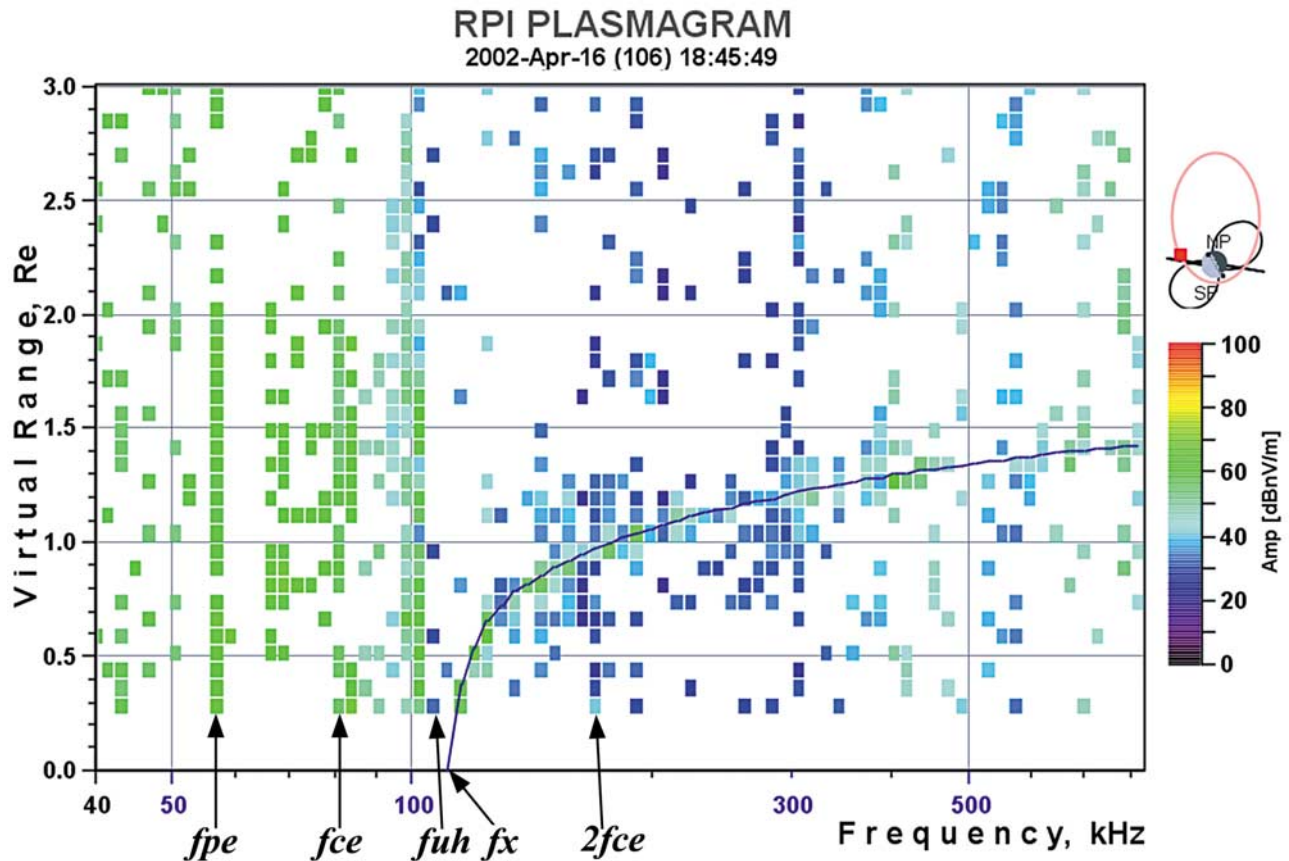


**Figure 1.** A plasmagram from IMAGE/RPI, showing signal amplitude dBnV/m as function of frequency and time delay expressed in terms of virtual range. A trace extending from  $\sim 111$  kHz to  $\sim 819$  kHz is formed from X mode echoes. Local electron plasma, electron cyclotron, and upper hybrid resonances are seen as vertical lines.  $f_x$  is the local X mode cutoff frequency.

underlying physical processes from measurements on a timescale never before possible.

### 3. Observations

[9] In this section we present observations by the IMAGE/RPI in the northern hemisphere made before and during a moderate magnetic storm, which started at about 1200 UT on 17 April 2002. The purpose of the present study is to examine the relation of the electron density distributions with the solar wind/IMF conditions. Therefore we select observations in prestorm and storm times when the solar wind/IMF conditions varied significantly. There are three periods during which multiple field-aligned density profiles are available to derive “two-dimensional” density images. These time periods are 1809–1906 UT on 16 April, 2221–2332 UT on 17 April, and 0732–0827 UT on 20 April 2002. Between these periods when the satellite flew through the same regions, the RPI provided too few density profiles to construct robust “two-dimensional” density images because the RPI often operated in other measurement programs. The footprints of the IMAGE orbit for these periods are shown in Figure 3 in corrected geomagnetic (CGM) coordinates [Hakura, 1965], in a dial plot of CGM latitude–magnetic local time (MLT) format. Throughout the paper, the latitudes and MLT are defined in CGM coordinates on the surface of the Earth unless otherwise indicated. The Tsyanenko 96

(T96) [Tsyanenko, 1995] magnetospheric magnetic field model is used to map the satellite orbit to the Earth’s surface. The passes discussed here are all close to noon sector and across the nominal dayside aurora/cusp latitudes, the regions of the boundary between open and closed field lines. All footprints of the three orbit segments were under sunlight (solar zenith angle  $< 72^\circ$ ) and the satellite flew from high to low latitudes. Figure 4 displays the variation of hourly Dst index from 15 April to 27 April 2002. Each vertical line roughly indicates the times of the IMAGE/RPI measurements used to construct a “two-dimensional” density image. The first period of the IMAGE/RPI observations was before the storm, the second one was in the temporal recover of the Dst, and the last one was at the peak of the storm when the hourly Dst dropped to about  $-148$  nT.

#### 3.1. Solar Wind/IMF Conditions

[10] Figure 5 displays the Dst index and solar wind/IMF parameters measured by the ACE satellite in the upstream solar wind on 16–17 April and on 20 April 2002. Plotted from top to bottom are Dst, IMF strength, IMF  $B_y$  and  $B_z$  components in GSM coordinates, solar wind proton density, solar wind velocity, and solar wind dynamic pressure, respectively. Using the solar wind velocity component along the Sun–Earth line, the three periods of IMAGE/RPI measurements, marked by three pairs of vertical lines in Dst panels, are backward shifted by the transit time for the solar

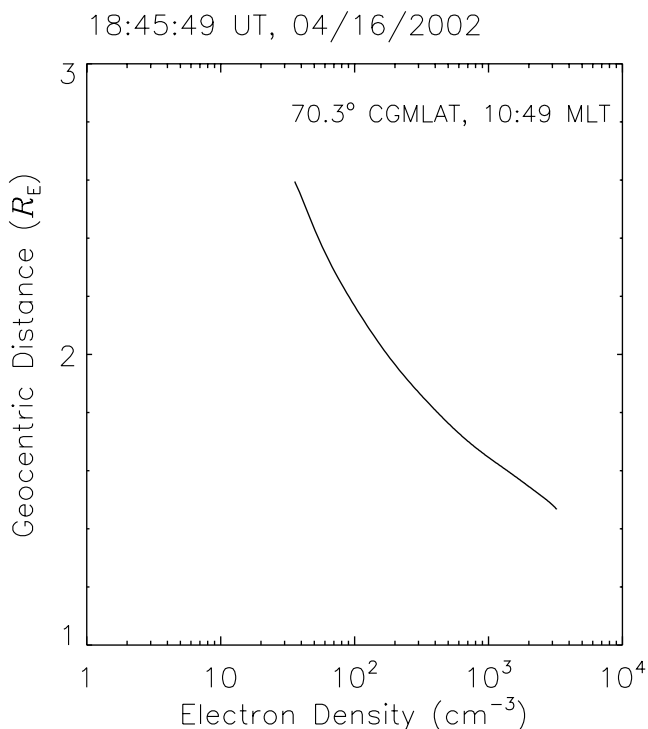


**Figure 2.** Field-aligned electron density profile calculated from the trace in the plasmagram in Figure 1.

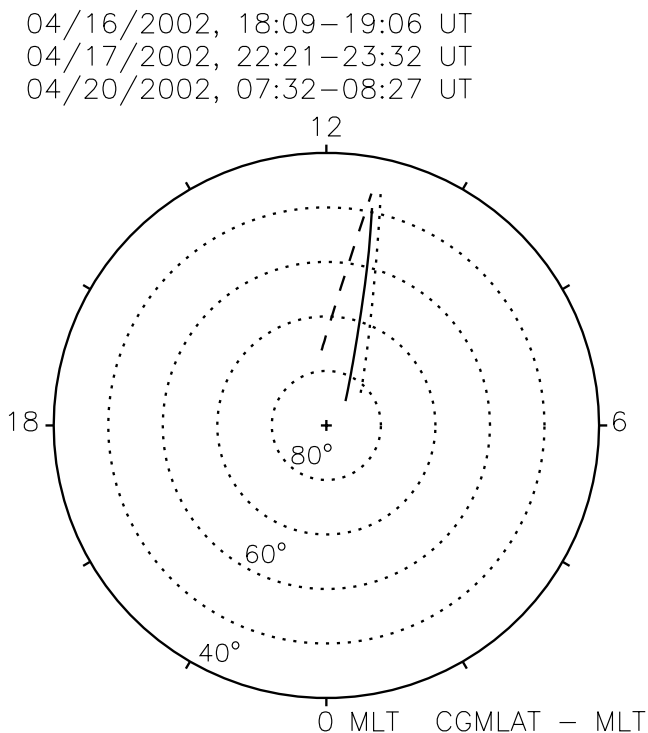


**Figure 3.** Footprints of the IMAGE orbits during 1809–1906 UT on 16 April (solid line), 2221–2332 UT on 17 April (dotted line), and 0732–0827 UT on 20 April (dashed line), in CGMLAT-MLT coordinates. The satellite orbits were from high to low latitudes.

wind to travel from the ACE location to the expected magnetopause ( $10.5 R_E$  in front of the Earth). The IMF  $B_z$  was southward for the first period of IMAGE/RPI measurements (1809–1906 UT of 16 April), with  $B_z$  of  $-3.3$  to  $-0.8$  nT. The  $B_y$  was negative (eastward), in the range of  $-5$  to  $-2$  nT. There is a data gap in the solar wind proton density during which the dynamic pressure cannot be calculated. If the proton density did not change much in the data gap, which was a reasonable assumption since there were no significant changes in the solar wind speed and IMF orientation, it would be about  $7 \text{ cm}^{-3}$  as inferred from later measurements. The solar wind dynamic pressure then would be about 2 nPa, typical for the solar wind dynamic pressure [Hundhausen, 1995].

[11] At about 1020 UT on 17 April, the IMF strength, proton density, solar wind velocity, and dynamic pressure increased steeply, indicating a shock passed the ACE satellite. The second pair of vertical lines mark the backward shifted start and end times of the second period of IMAGE/RPI measurements (2221–2332 UT of 17 April). The IMF  $B_z$  was slightly northward during the period and the dynamic pressure was moderately high, about 4–5 nPa. Before this period, the IMF  $B_z$  had been primarily positive for about 2 hours. In this period the IMF  $B_y$  was positive (westward), up to 10 nT.

[12] The third period of the RPI measurements (0732–0827 UT of 20 April) was under westward IMF  $B_y$  and southward IMF  $B_z$  (see the period within the third pair of vertical lines). The solar wind dynamic pressure was again moderately high, about 4 nPa. Except several short northward excursions, the IMF  $B_z$  had been strongly negative, as low as  $-20$  nT, for more than 6 hours. Owing to the persistent strong southward IMF  $B_z$ , the Dst experienced

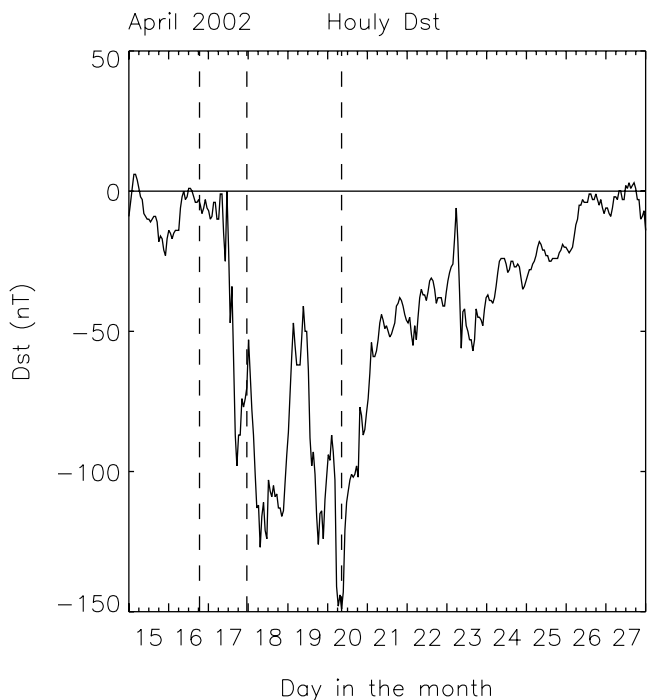


**Figure 4.** Dst variation during 15–27 April 2002. Each vertical line indicates the central time of the IMAGE footprint segment shown in Figure 3.

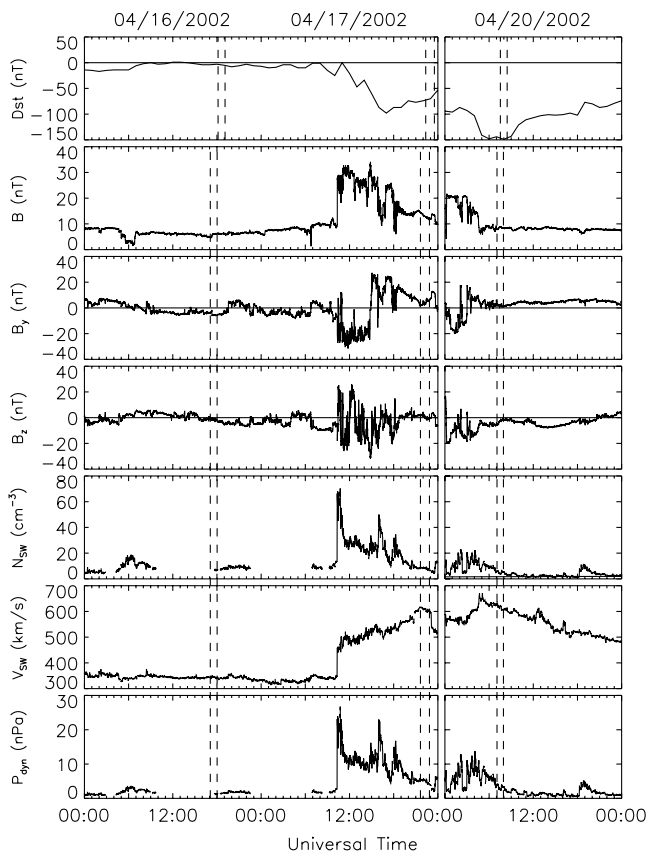


**Figure 5.** IMF strength, IMF  $B_y$  and  $B_z$  components, solar wind proton density, solar wind velocity, and dynamic pressure measured by the ACE satellite at GSM-X =  $\sim 223 R_E$  during (left) 16–17 April 2002 and (right) 20 April 2002. Hourly  $Dst$  index is also plotted for comparison. Three pairs of vertical lines in  $Dst$  panels mark three periods of the RPI measurements shown in Figure 6. In solar wind/IMF panels, those periods are backward shifted using the estimated transit time for the solar wind to travel from the ACE location to the magnetopause.

another decrease starting at about 0000 UT on 20 April and dropped to below  $-148$  nT at about 0700 UT on 20 April.

### 3.2. Two-Dimensional Density Images

[13] In Figure 6 we show the “two-dimensional” density images projected onto the solar magnetic (SM)  $X_{SM}$ - $Z_{SM}$  plane for the three periods mentioned previously. The left panel shows the electron density image from  $84.3^\circ$  to  $49.3^\circ$  CGM latitude, derived from individual field-aligned density profiles measured by the RPI from 1809 to 1906 UT on 16 April 2002. Several regions of different plasma density characteristics can be identified from this density distribution. High electron densities are seen in the region below  $\sim 54^\circ$  ( $L < 2.9$ , region of red color), with densities greater than  $2600 \text{ cm}^{-3}$  at the satellite locations ( $\sim 1 R_E$  altitude). This region is inside the plasmasphere. The densities decrease rapidly and keep above this latitude decreasing along the satellite orbit because of the density decrease due to the increase in radial distance and/or latitude, as will be seen in Figure 7. Such continuous density decrease makes the identification of the plasmopause difficult. Neverthe-

less, we will show later that the field line of CGM latitude  $65.2^\circ$  ( $L = 5.3$ ) may be used to delimit two adjacent regions of different radial distance dependence of the densities and distinct plasma flow characteristics. Therefore we tentatively define  $L = 5.3$  as the boundary, or the plasmopause, separating the plasmasphere from the plasma trough. The density distributions in the plasmasphere display two layers: one high-density region mentioned above, and a high  $L$ -value region with lower densities. It will be also shown that the region of greater  $L$  value is the outer plasmasphere within which the flux tubes are still experiencing refilling of the plasma from the underlying ionosphere.

[14] The density variations along the satellite orbit can also be determined by the upper hybrid resonance (UHR) noise band observed in RPI passive mode measurements. The UHR noise band is a narrow band of signal intensity enhancements bounded by the local hybrid resonance frequency ( $f_{uh}$ ) and electron plasma frequency ( $f_{pe}$ ) [e.g., Mosier *et al.*, 1973]. It is a typical feature of RPI passive spectrum measurements when the electron cyclotron frequency ( $f_{ce}$ ) is smaller than the  $f_{pe}$ . Figure 7 shows three dynamic spectra, for 1730–1930 UT on 16 April, 2200–2400 UT on 17 April, and 0700–0900 UT on 20 April 2002. In each dynamic spectrum, the UHR noise signature is visible and decreases dramatically in frequency (from right to left, i.e., from low to high latitude) at the time indicated by a vertical arrow. The sharp decrease of the frequency of the UHR band indicates a steep gradient of the plasma density since  $N_e \propto f_{pe}^2$ . For the period of 1730–1930 UT on 16 April 2002, the sharp decrease occurred at about 1902 UT when the IMAGE crossed  $\sim 54^\circ$  CGM latitude. The UHR band continued to drop quickly in frequency from low to high latitude beyond  $\sim 54^\circ$ , consistent with the density variations seen in the “two-dimensional” density image (left panel of Figure 6).

[15] Beyond the plasmopause marked by the field line of  $65.2^\circ$  in the left panel of Figure 6, the in situ densities decrease to lower than  $100 \text{ cm}^{-3}$ . This is the low-density plasma trough. It is remarkable that there is a V-shaped density depletion extending from about  $73.8^\circ$  to  $78^\circ$  in latitude. The density is below  $\sim 20 \text{ cm}^{-3}$  in the depletion region and the minimum density is about  $7 \text{ cm}^{-3}$ . The poleward boundary of this region is along the field line of  $\sim 78^\circ$  CGM latitude and extends down to about  $2.5 R_E$  radial distance. The low-density structure in the plasma trough is possibly in the region close to or even partially overlapped with the auroral oval. For this period, the auroral images obtained by the far ultraviolet (FUV) imager [Mende *et al.*, 2000] on IMAGE show faint auroral emissions (images not shown) on the dayside so that it is difficult to locate the boundaries of the dayside auroral oval. However, there is a density enhancement in a narrow latitude range ( $78^\circ$ – $79.2^\circ$ ), just poleward of the density depletion. This density enhancement may be the signature of the cusp where both precipitating magnetosheath plasma and enhanced ion outflows can cause relative high densities in the cusp proper [e.g., Lockwood *et al.*, 1985; Horwitz and Lockwood, 1985; Smith and Lockwood, 1996; André and Yau, 1997]. We associate the density enhancement observed in the present period with the cusp because of its narrow latitude range,  $\sim 1^\circ$ , typical of the latitudinal width of the cusp, and the distinct plasma flow characteristics as will be

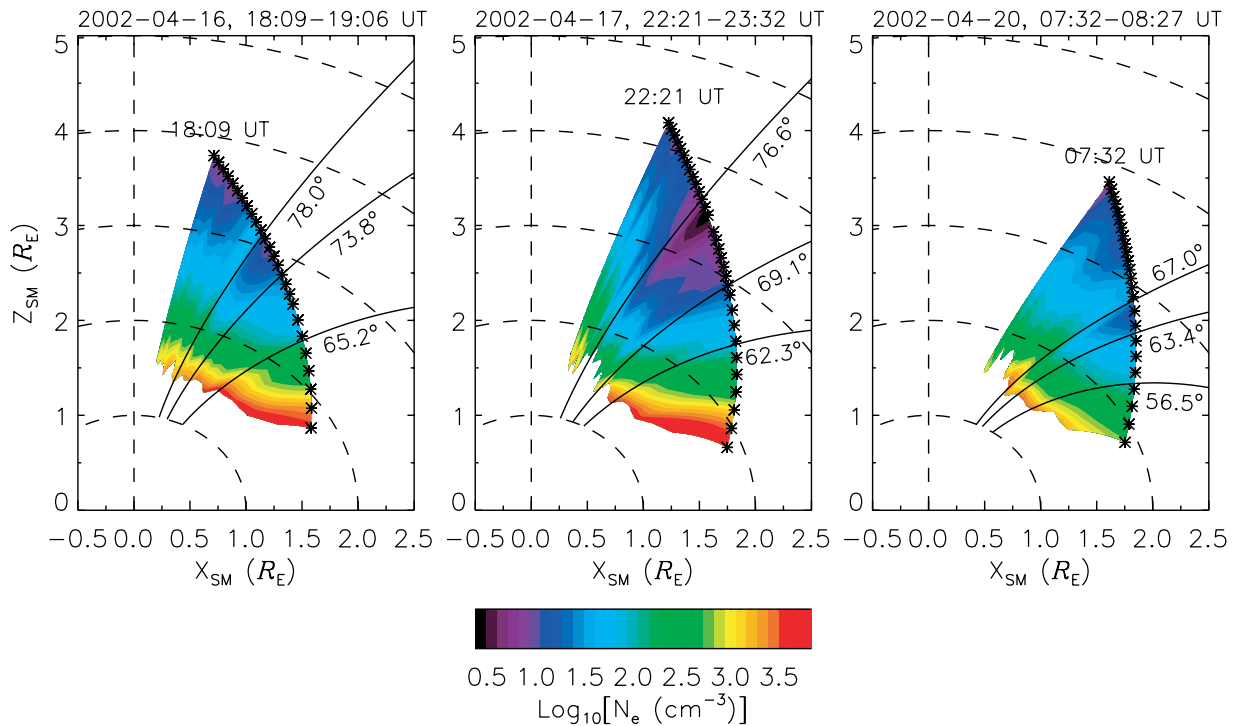


**Figure 6.** Two-dimensional (2-D) electron density ( $N_e$ ) images projected onto the solar magnetic  $X_{SM}$ - $Z_{SM}$  plane. The 2-D images are derived from the field-aligned density profiles measured by the RPI from 1809 to 1906 UT on 16 April, 2221 to 2332 UT on 17 April, and 0732 to 0827 UT on 20 April, respectively. The stars on each orbit segment indicate the locations from which the field-aligned density profiles were measured. Also plotted are three field lines (solid) with the CGM latitude labeled. The field line of lowest latitude indicates the plasmopause, while the other two field lines limit density depletion region. See text for details.

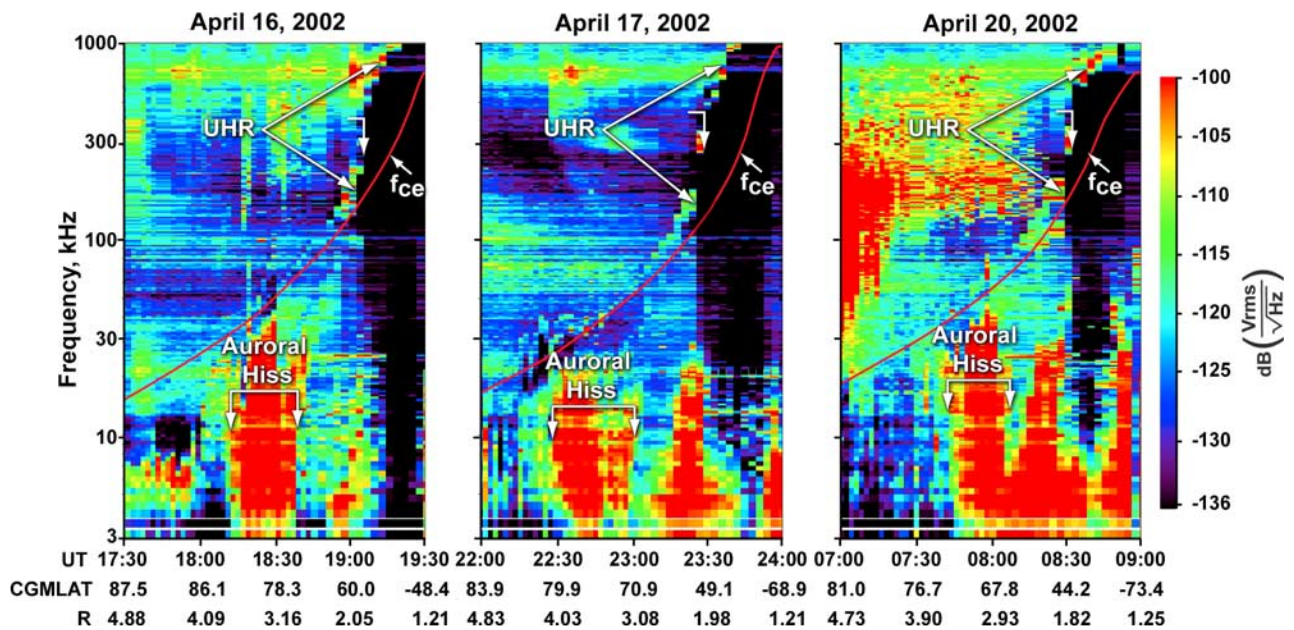


**Figure 7.** The IMAGE/RPI dynamic spectral image showing the plasma wave environment along the satellite orbits for the periods of 1730–1930 UT on 16 April, 2200–2400 UT on 17 April, and 0700–0900 UT on 20 April 2002. The auroral hiss noise and upper hybrid resonance (UHR) noise band are indicated in each spectrum. Down-pointing vertical arrows indicate the starting time (location) of the sharp frequency change of the UHR band. Red line is local electron cyclotron frequency derived from the RPI active sounding. Universal time (UT), CGM latitude, and radial distance ( $R$ ) along the orbits are labeled under the abscissa.

seen later in Figure 11. If this is the case, then the density depletion must be at least partially over the auroral oval because the cusp is immediately poleward of the dayside auroral oval under southward IMF  $B_z$  condition [e.g., *Smith and Lockwood, 1996*].

[16] The density depletion that occurred from 1831 to 1841 UT ( $78^\circ$  to  $73.8^\circ$ ), coincides with the equatorward part of the intense broadband emissions below the electron cyclotron frequency (see left panel of Figure 7). Previous observations have established that such emissions at high latitudes are whistler mode auroral hiss [e.g., *Labelle and Treumann, 2002*, and references therein]. It is possible that the auroral hiss is generated at radial distance of  $2.7$ – $2.9 R_E$  in the auroral current region and propagates both poleward and equatorward from its source region [e.g., *Gurnett et al., 1983*]. However, our data set does not contain enough information for us to further study the possible relationship between the density depletion and the auroral hiss.

[17] During the partial recovery phase of the Dst when the IMF  $B_z$  has been northward for 2 hours, the electron densities in the IMAGE orbit plane demonstrate quite a different picture. The middle panel of Figure 6 displays the density image between  $81.3^\circ$  and  $46^\circ$  CGM latitude, derived from the RPI measurements from 2221 to 2332 UT on 17 April 2002. A remarkable change compared to the density image in the left panel is that the density depletion expanded to wider latitude range and extended to lower altitude, as marked by the field lines of  $69.1^\circ$  and  $76.6^\circ$ . The density depletion corresponds again to the equatorward part of intense auroral hiss emissions displayed in the middle panel of Figure 7. The auroral images taken by the IMAGE/FUV during this period (images not shown) do not display clear auroral oval on the dayside, preventing us from identifying the locations of the boundaries of the dayside auroral oval. The densities in the depletion region are very low, with the lowest density  $\sim 2 \text{ cm}^{-3}$ . Like the previous period of the RPI measurements, the plasmopause, marked by the  $62.3^\circ$  CGM latitude field line ( $L = 4.57$ ), is identified as the boundary between adjacent regions of different radial distance dependence of the densities and distinct plasma flow characteristics. The plasmasphere also consists of two layers: the inner plasmasphere (believed to be in diffusive equilibrium) and the outer plasmasphere, in which the flux tubes were refilling with the plasma from the ionosphere, as will be discussed later.

[18] In this satellite pass, no localized density enhancement appears to be associated with the aurora/cusp poleward of the density depletion region. Instead, we will see from the middle panel of Figure 10 that the polar cap is possibly immediately poleward of the density depletion, i.e., at latitudes higher than  $76.6^\circ$ . The cusp was not observed because it might be located further poleward under northward IMF  $B_z$  [e.g., *Song et al., 2003*]. In addition, the cusp is much more localized during northward IMF  $B_z$  than during southward IMF  $B_z$  [*Smith and Lockwood, 1996*]. Thus it is possible that the IMAGE did not cross the cusp, especially as the positive IMF  $B_y$  shifted the cusp position postnoon while the IMAGE orbit was prenoon (see Figure 3).

[19] The third period of the RPI measurements from 0732 to 0827 UT on 20 April 2002 occurred in the period of persistent southward IMF  $B_z$ , which caused the Dst mini-

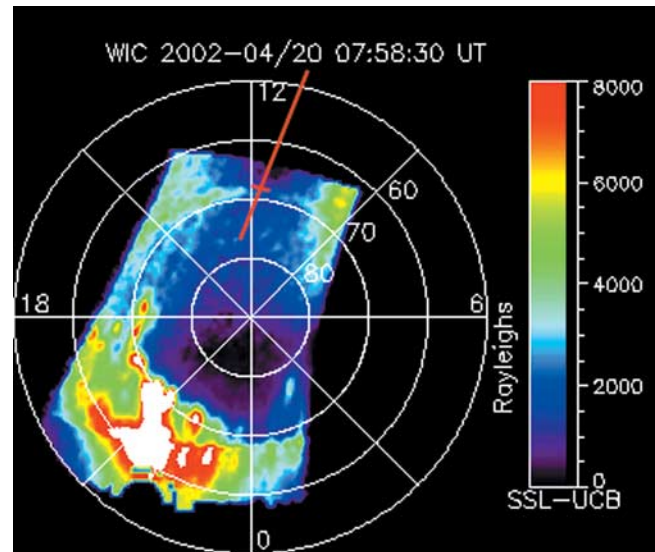


**Figure 8.** An auroral image from the IMAGE/FUV at 0758:30 UT on 20 April 2002. The footprints of the satellite orbit for the period of 0732–0827 UT on 20 April 2002 is overlotted as a red line. The auroral oval on the dayside is located roughly between  $67.5^\circ$  and  $70^\circ$  latitude. The satellite location at this time was at  $\sim 68.3^\circ$  latitude and 1144 MLT (marked by a short bar).

um of  $-148 \text{ nT}$  (see Figure 4). It is seen from the right panel of Figure 6 that the electron density image during this period is to some degrees similar to that in the first period of the RPI measurements shown in the left panel of Figure 6. The plasmasphere, however, was compressed by the increased magnetospheric convection associated with the strong southward IMF  $B_z$  and the plasmopause moved to lower latitude (lower  $L$  value). Again, the plasmopause, marked by the field line of CGM latitude  $56.5^\circ$  ( $L = 3.07$ ), is not clearly visible from the electron density image, but it will become identifiable in later plots showing the radial dependence of the densities and the inferred plasma flows. The density depletion (between  $\sim 63.4^\circ$  and  $\sim 67^\circ$ ) and the localized density enhancements (between  $\sim 67^\circ$  and  $\sim 70^\circ$ ) are still visible but shifted equatorward as well. In this case, the localized density enhancements are largely coincident with the auroral oval as identified from a series of IMAGE/FUV images taken from 0746 to 0800 UT on 20 April 2002 when the IMAGE flew through  $\sim 73^\circ$  to  $67^\circ$  CGM latitude. Therefore the auroral oval was poleward of the density depletion region for this period. As an example, a FUV image taken at 0758:30 UT is displayed in Figure 8. The coordinates in the FUV image are APEX geomagnetic coordinates [*Richmond, 1995*]. As noted by *Gasda and Richmond [1998]*, at auroral to polar cap latitudes the APEX latitudes are essentially the same as the CGM latitudes: the maximum difference between the APEX latitude at 110 km altitude and CGM latitude at ground level is  $0.17^\circ$ . The satellite footprints for the period of 0732–0827 UT are overlotted on the FUV image with the satellite location at that time (at  $68.3^\circ$  and 1140 MLT) marked by a short bar. It is shown that the auroral oval was located roughly between  $67.5^\circ$  and  $69^\circ$  APEX latitude, poleward of the density depletion (between  $63.4^\circ$  and  $67^\circ$ ) and covered by the

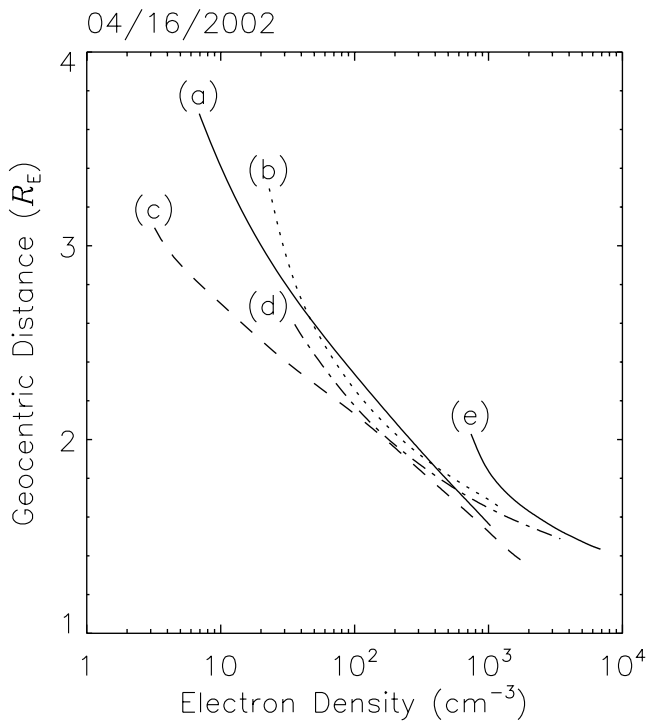


**Figure 9.** Sample field-aligned electron density profiles from (a) polar cap, (b) cusp, (c) density depletion region, (d) outer plasmasphere, and (e) inner plasmasphere. The density profiles were from the first period of the RPI measurements.

density enhancements ( $67^{\circ}$ – $70^{\circ}$ ). The most poleward part of the density enhancements ( $69^{\circ}$ – $70^{\circ}$ ) probably corresponds to the cusp.

[20] It can be seen in Figure 6 that the densities in different regions have distinct radial distance dependence along the field lines. This is clearly demonstrated by Figure 9, in which we plot the sample field-aligned density profiles from various plasma regions for the first period of the RPI measurements. It is shown that the plasmaspheric densities show the smallest variation with the radial distance along the field line while the density gradient in the density depletion region is largest. The statistical study of *Nsumei et al.* [2003] showed that the polar cap densities have a power law relation with an exponent index of about  $-5$  with the radial distance. Since the densities in different plasma regions have distinct radial distance dependence, normalizing the densities with  $r^{-5}$ , where  $r$  is the radial distance along individual field lines, helps better differentiate the plasma regions relative to the polar cap. In Figure 10 we present distributions of the densities divided by  $r^{-5}$ . It is clear that different plasma regions are indeed better delimited. In Figure 6 we have marked the plasmapause with the field line of CGM latitude  $65.2^{\circ}$ ,  $62.3^{\circ}$ , and  $56.5^{\circ}$ , respectively, from left to right. In that figure the plasmapause is not clearly identifiable. Figure 10 demonstrates that these field lines are roughly the boundaries that separate adjacent regions of different radial distance dependence of the densities along the field lines. The normalized densities in the plasma trough region decrease with radial distance along the field lines, indicating a density decrease faster than  $r^{-5}$ . The normalized densities in the plasmasphere are more smoothly distributed along the field lines, particularly

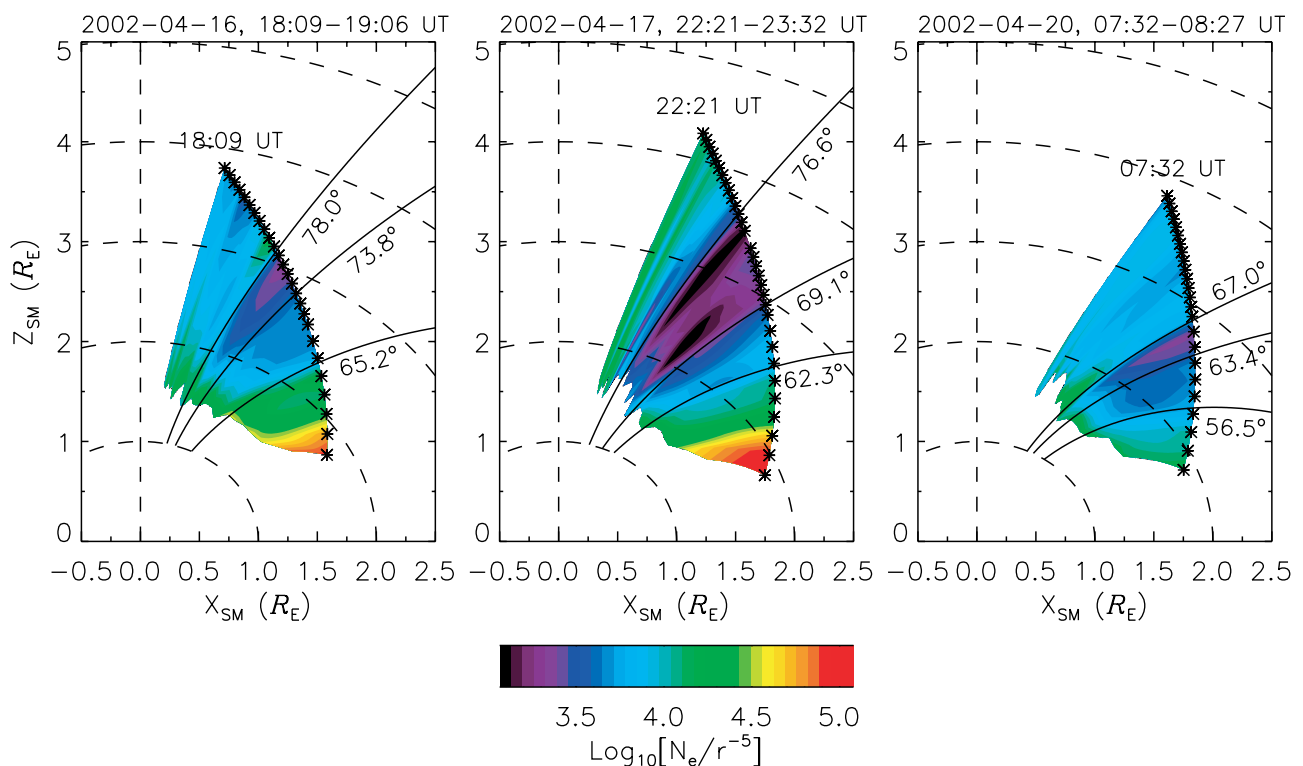


**Figure 10.** Same format as Figure 6 but for electron density images divided by  $r^{-5}$ , where  $r$  is the radial distance (in  $R_E$ ) along individual field lines.

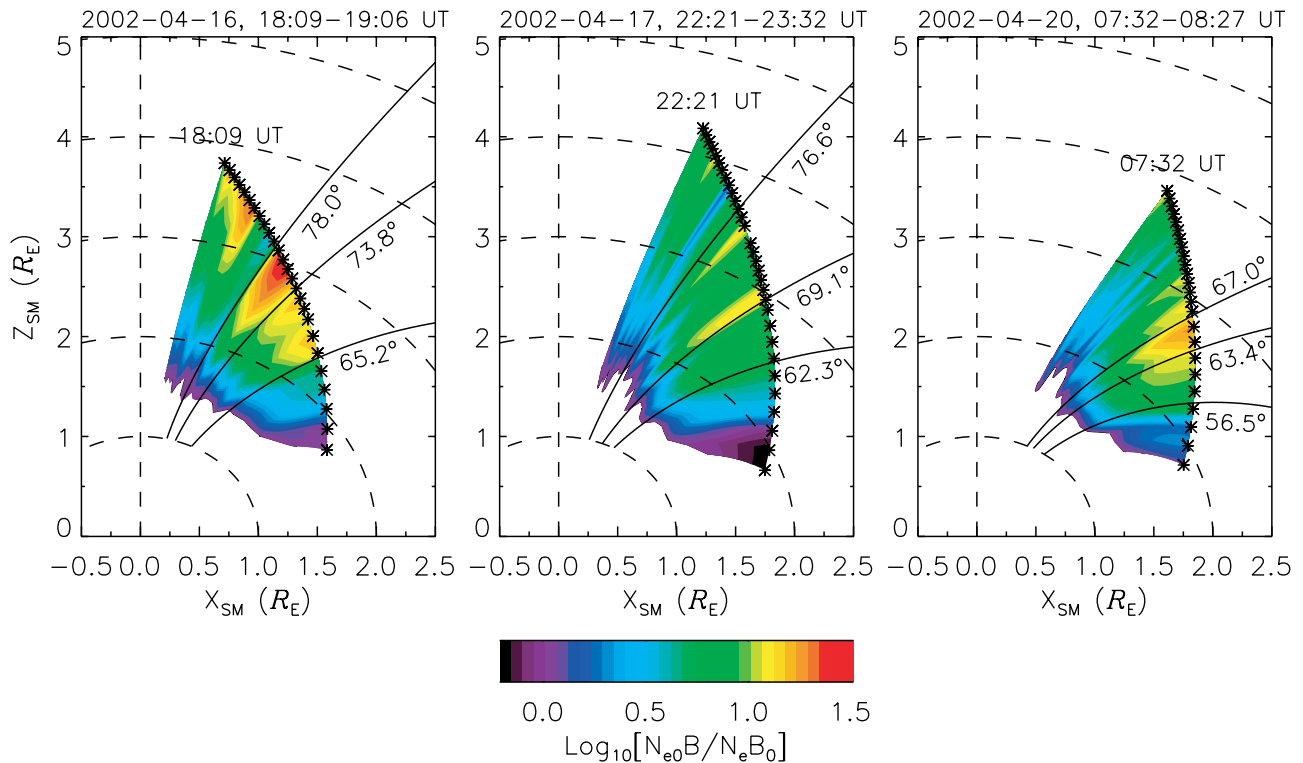


**Figure 11.** Same format as Figure 6 but for  $N_{e0}B/N_eB_0$ , where  $N_{e0}$  and  $B_0$  are the electron density and magnetic field at the bottom of the individual field-aligned density profiles.

in the inner plasmasphere. However, the plasmaspheric density variations along the field lines result from the combined effects of the radial distance and latitude changes. We thus cannot conclude that the plasmaspheric density has a  $r^{-5}$  dependence on the radial distance from the smooth variations of the normalized densities.

[21] In the middle panel of Figure 10, the polar cap is identified as the region immediately poleward of the density depletion because of the uniform radial distance variation of the normalized densities. Note that at high latitudes the field lines are close to aligned with the radial direction. In all three panels the normalized densities are more uniformly distributed with the radial distance in the polar cap than in the plasma trough since the electron densities in the polar cap vary with the radial distance in a way closer to  $r^{-5}$ .

### 3.3. Inferred Plasma Flow Characteristics

[22] The instantaneously measured field-aligned density profiles by the IMAGE/RPI provide the information of the density gradient along the field lines, which is not available from in situ density measurements. In this section we use the density gradient to infer the characteristics of the plasma flows in various plasma regions and thus get insight into the plasma dynamics in response to the solar wind.

[23] In the altitude range of the present RPI observations, there is essentially no production and loss of the charged particles. If neglecting the plasma transport perpendicular to magnetic field lines, the continuity equation can be written as

$$\frac{\partial N_e}{\partial t} + B \frac{\partial}{\partial s} \left( \frac{N_e v}{B} \right) = 0, \quad (1)$$

where  $N_e$  is the electron density,  $B$  is the magnetic field and  $v$  is the field-aligned electron velocity, and  $s$  is the arc length along a field line. When there is no or weak field-aligned current,  $v$  is the average field-aligned velocity of all ion species since  $v = (\sum_i v_i N_i - J/e)/N_e$ , where  $N_i$  and  $v_i$  is the ion density and field-aligned velocity, respectively,  $J$  is the field-aligned current density, and  $e$  is the elementary charge. In the case of quasi-steady state or slow time variation of the density, we have  $N_e v/B = \text{const}$ . In Figure 11 we plot the distributions of  $v/v_0 = N_{e0}B/N_eB_0$ , the normalized field-aligned velocities. The variables with subscript 0 are those at the bottom of the individual density profiles measured by the IMAGE/RPI. Although the steady-state approximation may not be perfect and perpendicular plasma transport may not be completely ignorable, we can obtain useful information regarding the plasma dynamics by examining such normalized velocities.

[24] Before we proceed with our discussion, we point out that because  $v_0$  is different for each individual density profile, only the change of the normalized velocities is relevant: the larger values of the normalized velocities only mean the larger change of the velocities along the individual field lines. In addition, the variation of the normalized velocities is along the field lines but it is often referred to as the altitudinal variation in the high-latitude regions because of the nearly vertical field lines. We also point out that the velocities along the field lines may be downward (negative  $v_0$ ). However, previous observations have shown that the plasma flows are generally upward along the field lines beyond the plasmopause, particularly during day time when the ionospheric ions are driven upward by the pressure gradient [e.g., *Sojka et al.*, 1983]. The observed

flow velocity increases along the field lines are larger than velocity increases associated with the adiabatic decrease of the plasma pitch angle, and the flow velocities are often supersonic (polar wind characteristic) [Singh and Horwitz, 1992; Moore *et al.*, 1999, and references therein].

[25] We first examine the left panel of Figure 11. There are two regions of slightly different flow characteristics in the plasmasphere. At lower latitudes or lower  $L$  shells, the normalized velocities are almost constant along the field lines suggesting that this is the inner plasmasphere with plasma in diffusive equilibrium. Meanwhile, the change in the normalized velocities along the field lines is significant in the outer region. Although the variations of the normalized velocities in the outer region may be the decrease of the downward flow velocities, it is reasonable to interpret such variations as the upward flowing of the ionospheric plasma, as discussed in, for example, the review paper of Singh and Horwitz [1992]. Therefore the flux tubes in the outer region are still experiencing refilling of the plasma from the ionosphere.

[26] Beyond the plasmopause, in the trough region, the normalized velocities rapidly increase along the field lines at altitudes above about  $1 R_E$ , indicating there is possible plasma acceleration above this altitude. The largest altitude increase in the normalized velocities is seen in the density depletion region, which possibly overlaps partially with the auroral oval for this period of measurements, as stated previously. The altitude variations of the normalized velocities display more structures in the aurora/cusp and polar cap. The normalized velocities in the region corresponding to the density enhancement seen in the left panel of Figure 6 vary relatively smoothly. If it is the cusp, as argued before, we have a simple explanation for such smooth variations of the normalized velocities: Strong heating and upward acceleration of plasma are expected in the cusp [e.g., Moore *et al.*, 1999, and references therein]. Meanwhile, the precipitating magnetosheath plasma balances the velocities of upward flowing ionospheric plasma in the normalized velocities. The large altitude increase of the normalized velocities in the region close to the poleward boundary of the cusp is due to the spread of the energized ions from the aurora zone/cusp to the polar cap by the antisunward convection for southward IMF [e.g., Lockwood *et al.*, 1985; André and Yau, 1997; Tu *et al.*, 2005].

[27] In the middle panel of Figure 11, the normalized velocities slightly decrease with altitude along the field lines in the inner plasmasphere where the densities are high, also suggesting that the inner plasmasphere was in diffusive equilibrium. The velocity appreciably changes along the field lines in the outer plasmasphere, again indicating possible plasma refilling from the ionosphere. The largest altitude increase in the normalized velocities is seen in the plasma trough for this period of the RPI measurements but the normalized velocities display more structures. Under the northward IMF  $B_z$ , the convection and auroral emission patterns are much more complicated than those during the southward IMF  $B_z$ . This is possibly the reason that the spread of the energized plasma from the aurora oval to the polar cap is not seen and the altitudinal increase of the normalized velocities is smaller in the polar cap.

[28] The right panel is for the last period of the RPI measurements. In the inner plasmasphere, variation in the

normalized velocities along the field lines is small, implying this is the region with the plasma in diffusive equilibrium. Note that the outer region of the plasmasphere where the normalized velocities display visible changes along the field lines is in a narrow region because of the overall compression of the plasmasphere. The largest increase of the normalized velocities with the radial distance is again seen in the density depletion region, which is to large extent at subauroral latitudes (see discussion in section 3.2). The cusp is possibly just poleward of the auroral oval with a weaker increase of the normalized velocities along the field lines. Further poleward, the increase in the normalized velocities along the field lines become even weaker, due to the spread of the energized ions from the aurora/cusp [e.g., Tu *et al.*, 2005].

#### 4. Summary and Discussion

[29] Using multiple field-aligned electron density profiles measured by the IMAGE/RPI, we have constructed “two-dimensional” density images in the middle- and high-latitude dayside inner magnetosphere for different solar wind/IMF conditions. This allows regions of different plasma characteristics, namely the plasmasphere, plasma trough, density depletion, aurora/cusp, and polar cap, to be identified along satellite orbit and the field lines. It is shown that the densities in various regions and the location of those plasma regions vary in accordance with the solar wind/IMF conditions. During the partial recovery of the Dst when the IMF  $B_z$  was northward, the density depletion region widens in latitude and extends to lower altitudes. Also, the plasma trough densities are lower during northward IMF and there is no signature of the cusp. When the IMF  $B_z$  had been strongly southward for several hours, the Dst reached a minimum and all the plasma regions moved to lower latitudes. Table 1 lists solar wind/IMF parameters during the periods of the RPI measurements (backward shifted with the solar wind transient time) and latitude range of those plasma regions for three periods of the RPI measurements. This table helps to clarify the relation between the locations of the plasma regions and the solar wind/IMF conditions for the cases considered.

[30] We have also used the density gradients along the field lines to examine the plasma flows. Although the assumption of steady state and neglecting the perpendicular plasma transport may not perfectly apply, the inferred characteristics of the plasma flows and underlying dynamics for each region under different solar wind/IMF conditions are reasonable. For instance, the weak variation of the flow velocities in the inner plasmasphere is understandable since there is diffusive equilibrium established. The inner plasmasphere in the diffusive equilibrium and the outer plasmasphere, possibly still experiencing refilling of the plasma, can be distinguished in the density images. The large increase of the plasma velocities in the auroral oval is also expected because of the strong auroral acceleration and heating of the plasma.

[31] In the past, electron density distributions were typically studied using a very large set of in situ density measurements that are averaged in specified spatial bins. The large variation in the location of the plasma regions under different solar wind/IMF conditions implies that we must be cautious in interpreting these types of average

**Table 1.** Solar Wind/IMF Parameters During the RPI Measurements (With Solar Wind Transient Time Considered), and Latitude Range of Plasma Regions for Three Periods Shown in Figure 6<sup>a</sup>

Date	Solar Wind/IMF					Latitude Range			
	$N_{SW}^b$	$V_{SW}^b$	$P_{dyn}^b$	$B_y$	$B_z$	PS	PT	DP	Cusp/PC
04/16/2002	~7 <sup>c</sup>	~420	~2 <sup>c</sup>	-5 - -2	-3.3 - -0.8	<65.2°	65.2°–73.8°	73.8°–78.0°	>78.0°
04/17/2002	~8	~600	~4.5	2 - 10	0.2 - 3	<62.3°	62.3°–69.1°	69.1°–76.6	>76.6°
04/20/2002	~6	~635	~4	1.2 - 6	-6 - -2	<56.5°	56.5°–63.4°	63.4°–67.0°	>67.0°

<sup>a</sup>PS is plasmasphere; PT is plasma trough; DP is density depletion; PC is polar cap.

<sup>b</sup>Solar wind proton density  $N_{SW}$  in  $\text{cm}^{-3}$ , velocity  $V_{SW}$  in km/s, and dynamic pressure  $P_{dyn}$  in nPa.

<sup>c</sup>Inferred value. See section 3.1 for detail.

electron density distributions. For example, *Palmroth et al.* [2001] noted that the variation in the cusp positions under different solar wind conditions likely spreads out the cusp signature in average density distributions. Therefore it is necessary to include the solar wind/IMF effects in future statistical studies using a large set of density measurements.

[32] The variations of the density distributions, seen in our images, appear to be primarily associated with the change of the IMF orientation and correspondingly different states of the magnetosphere. For instance, the density images in the second and last period of the RPI measurements were quite different from one another, most likely because of the intervening storm emptying the outer plasmasphere. However, the solar wind velocities and proton densities, and thus the dynamic pressures as well as IMF  $B_y$ , were similar in the two periods except that the IMF  $B_z$  had opposite orientations, as can be seen from Table 1. The density images in the first and last period were similar even though the solar wind conditions and IMF  $B_y$  orientation were different. The shift of the various plasma regions to lower  $L$  shells in the last period density image was primarily due to strong and persistent negative IMF  $B_z$ , which also caused the drop of the Dst from  $-94$  nT to  $-148$  nT in about 7 hours. These observations suggest that the controlling factor for density variations imaged by the RPI is the IMF  $B_z$  orientation for the case considered here. However, more cases are needed to examine before we reach definite conclusion on how the solar wind and IMF conditions affect the density distributions.

[33] In previous studies the in situ plasma density measurements were used to identify various plasma regions [e.g., *Marklund et al.*, 1990; *Carpenter and Anderson*, 1992; *Laakso and Grard*, 2002]. The IMAGE/RPI observations provide the ability to identify plasma regions more reliably because “two-dimensional” spatial extension of them can be seen. Furthermore, the difference in the radial distance dependence of the densities along the field lines in these regions can be determined using the near instantaneously measured field-aligned density profiles. Therefore different plasma regions are better differentiated, as has been shown in the normalized density images of Figure 10.

[34] It has been shown that the density depletion is the region with strongest plasma acceleration along the field lines. Figure 11 shows that the strong plasma acceleration primarily occurs at altitudes above  $1 R_E$ . We may conjecture that the density depletion resulted from the plasma escape to high altitudes caused by the strong plasma acceleration above  $1 R_E$  altitude and the insufficient supply of the plasma from ionospheric altitudes to compensate the plasma escape. Note that the density depletion

region is beyond the plasmopause. The escaped plasma is convected to the outer magnetosphere and eventually to the solar wind at the magnetopause. Most likely, the density depletion region partially overlapped the dayside auroral oval in the first period of measurements, as argued before, while it was at subauroral latitudes in the last period of measurements. In the auroral oval, the strong plasma acceleration at high altitudes can be caused by the wave heating and/or a large potential drop along the field lines [e.g., *André and Yau*, 1997; *Moore et al.*, 1999]. At subauroral latitudes, the density depletion observed by the RPI in the last period of measurements must have been produced by mechanisms different from those responsible for the formation of the subauroral ionospheric trough at low altitudes [e.g., *Roger et al.*, 1992]. It has also been noted that the density depletion is coincident with the equatorward part of the auroral hiss emissions, suggesting the possible link of the auroral hiss and the density depletion on the dayside.

[35] The present observations also demonstrate that the densities in the polar cap vary with the radial distance in a way close to  $r^{-5}$ , implying that there is rapid increase of the plasma velocities upward along the field lines in the polar cap [*Nsumei et al.*, 2003]. In the region of the poleward boundary of the dayside aurora/cusp, such a velocity increase may be accomplished through the spread of the energized ions, particularly  $O^+$ , from its acceleration region in the aurora/cusp when the convection is antisunward [e.g., *Lockwood et al.*, 1985; *Tsunoda et al.*, 1989; *Tu et al.*, 2005]. The progressively weaker increase of the normalized velocities poleward of the aurora/cusp displayed in the left and right panels of Figure 11 may be the signature of the spread of the energized ions from the aurora/cusp to the polar cap. Note that in the polar cap the electron velocity is the average velocity of all ion species because there are essentially no field-aligned currents. In the polar cap the ions are also locally accelerated upward by the ambipolar electric fields (most effective for light ions like  $H^+$  and  $He^+$  ions) [e.g., *Axford*, 1968]. Nevertheless, it is necessary to perform more detailed observations, combined with simulations, to quantitatively explain how such radial distance dependence is produced in the polar cap.

[36] **Acknowledgments.** This work was supported by NASA under subcontract 83822 from Southwest Research Institute and by NSF grant NSF-ATM 0518227 to the University of Massachusetts Lowell. We thank the efforts of ACE team (magnetic field experiment PI: N. Ness at Bartol Research Institute and solar wind experiment PI: D. J. McComas at Southwest Research Institute) for making ACE level 2 IMF and solar wind data available at Coordinate Data Analysis Website (CDAWeb). The World Data Center for Geomagnetism (WDC-C2) at Kyoto University, Japan is acknowledged for providing the Dst data. We acknowledge I. A. Galkin and

G. Khmyrov for the BinBrowser analysis support. J.-N Tu thanks V. M. Vasyliūnas for his suggestions and comments.

[37] Arthur Richmond thanks the reviewers for their assistance in evaluating this paper.

## References

- André, M., and A. W. Yau (1997), Theories and observations of ion energization and outflow in the high latitude magnetosphere, *Space Sci. Rev.*, *80*, 27–48.
- Axford, W. I. (1968), The polar wind and the terrestrial helium budget, *J. Geophys. Res.*, *73*, 6855–6859.
- Burch, J. L., et al. (2001), Views of Earth's magnetosphere with the IMAGE satellite, *Science*, *291*(5504), 619.
- Carpenter, D. L., and R. R. Anderson (1992), An ISEE/whistler model of equatorial electron density in the magnetosphere, *J. Geophys. Res.*, *97*, 1097–1108.
- Chandler, M. O., J. H. Waite Jr., and T. E. Moore (1991), Observations of polar ion outflows, *J. Geophys. Res.*, *96*, 1421–1428.
- Denton, R. E., J. Goldstein, and J. D. Menietti (2002), Field line dependence of magnetospheric electron density, *Geophys. Res. Lett.*, *29*(24), 2205, doi:10.1029/2002GL015963.
- Denton, R. E., J. D. Menietti, J. Goldstein, S. L. Young, and R. R. Anderson (2004), Electron density in the magnetosphere, *J. Geophys. Res.*, *109*, A09215, doi:10.1029/2003JA010245.
- Fung, S. F., and J. L. Green (2005), Modeling of field-aligned radio echoes in the plasmasphere, *J. Geophys. Res.*, *110*, A01210, doi:10.1029/2004JA010658.
- Gallagher, D. L., P. D. Craven, and R. H. Comfort (2000), Global core plasma model, *J. Geophys. Res.*, *105*, 18,819–18,833.
- Gasda, S., and A. D. Richmond (1998), Longitudinal and interhemispheric variations of auroral ionospheric electrodynamic in a realistic geomagnetic field, *J. Geophys. Res.*, *103*, 4011–4021.
- Goldstein, J., R. E. Denton, M. K. Hudson, E. G. Miftakhova, S. L. Young, J. D. Menietti, and D. L. Gallagher (2001), Latitudinal density dependence of magnetic field lines inferred from Polar plasma wave data, *J. Geophys. Res.*, *106*, 6195–6201.
- Green, J. L., et al. (2000), Radio plasma imager simulations and measurements, *Space Sci. Rev.*, *91*, 361–389.
- Green, J. L., S. Boardson, S. F. Fung, H. Matsumoto, K. Hashimoto, R. R. Anderson, B. R. Sandel, and B. W. Reinisch (2004), Association of kilometer continuum radiation with plasmaspheric structures, *J. Geophys. Res.*, *109*, A03203, doi:10.1029/2003JA010093.
- Gurnett, D. A., S. D. Shawhan, and R. R. Shaw (1983), Auroral hiss, Z mode radiation, and auroral kilometer radiation in the polar magnetosphere: DE 1 observations, *J. Geophys. Res.*, *88*, 329–340.
- Hakura, Y. (1965), Tables and maps of geomagnetic coordinates corrected by the higher order spherical harmonic terms, *Rep. Ionos. Space Res. Jpn.*, *19*, 121–157.
- Horwitz, J. L., and M. Lockwood (1985), The cleft ion fountain: A two-dimensional kinetic model, *J. Geophys. Res.*, *90*, 9749–9762.
- Huang, X., and B. W. Reinisch (1982), Automatic calculation of electron density profiles from digital ionograms: 2. True height inversion of topside ionograms with the profile-fitting method, *Radio Sci.*, *17*, 837–844.
- Huang, X., B. W. Reinisch, P. Song, J. L. Green, and D. L. Gallagher (2004), Developing an empirical density model of the plasmasphere using IMAGE/RPI observations, *Adv. Space Res.*, *33*, 829–833.
- Hundhausen, A. J. (1995), The solar wind, in *Introduction to Space Physics*, edited by M. G. Kivelson and C. T. Russell, pp. 92, Cambridge Univ. Press, New York.
- Johnson, M. T., and J. R. Wygant (2003), The correlation of plasma density distributions over 5000 km with solar illumination of the ionosphere: Solar cycle and zenith angle observations, *Geophys. Res. Lett.*, *30*(24), 2260, doi:10.1029/2003GL018175.
- Johnson, M. T., J. R. Wygant, C. Cattell, F. S. Mozer, M. Temerin, and J. Scudder (2001), Observations of the seasonal dependence of the thermal plasma density in the southern hemisphere auroral zone and polar cap at 1 RE, *J. Geophys. Res.*, *106*, 19,023–19,033.
- Laakso, H. L., and R. Grard (2002), The electron density distribution in the polar cap: Its variability with seasons, and its response to magnetic activity, in *Space Weather Study Using Multipoint Techniques, COSPAR Colloq. Ser.*, vol. 12, edited by L.-H. Lyu, pp. 193–202, Elsevier, New York.
- Labelle, J., and R. A. Treumann (2002), Auroral radio emissions, 1. Hisses, roars, and bursts, *Space Sci. Rev.*, *101*, 295–440.
- Lemaire, J., and K. I. Gringauz (1998), *The Earth's Plasmasphere*, Cambridge Univ. Press, New York.
- Lockwood, M., M. O. Chandler, J. L. Horwitz, J. H. Waite Jr., T. E. Moore, and C. R. Chappell (1985), The cleft ion fountain, *J. Geophys. Res.*, *90*, 9736–9748.
- Marklund, G. T., L. G. Blomberg, C.-G. Fälthammar, R. E. Erlandson, and T. A. Potemra (1990), Signatures of the high-altitude polar cusp and dayside auroral regions as seen by the Viking electric field experiment, *J. Geophys. Res.*, *95*, 5767–5780.
- Mende, S. B., et al. (2000), Far ultraviolet imaging from the IMAGE spacecraft: 2. Wideband FUV imaging, *Space Sci. Rev.*, *91*, 271–285.
- Moore, T. E., R. Lundin, D. Alcayde, M. André, S. B. Ganguli, M. Temerin, and A. Yau (1999), Source processes in the high-latitude ionosphere, in *Magnetospheric Plasma Sources and Losses*, edited by B. Hultqvist et al., pp. 7–84, Springer, New York.
- Mosier, S. R., M. L. Kaiser, and L. W. Brown (1973), Observations of noise bands associated with the upper hybrid resonance by the IMP 6 radio astronomy experiment, *J. Geophys. Res.*, *78*, 1673–1679.
- Nsumei, P. A., X. Huang, B. W. Reinisch, P. Song, V. M. Vasyliūnas, J. L. Green, S. F. Fung, R. F. Benson, and D. L. Gallagher (2003), Electron density distribution over the northern polar region deduced from IMAGE/radio plasma imager sounding, *J. Geophys. Res.*, *108*(A2), 1078, doi:10.1029/2002JA009616.
- Palmroth, M., H. Laakso, and T. I. Pulkkinen (2001), Location of high-altitude cusp during steady solar wind conditions, *J. Geophys. Res.*, *106*, 21,109–21,122.
- Persoon, A. M., D. A. Gurnett, and S. D. Shawhan (1983), Polar cap electron densities from DE 1 plasma wave observations, *J. Geophys. Res.*, *88*, 10,123–10,136.
- Reinisch, B. W., et al. (2000), The Radio Plasma Imager investigation on the IMAGE spacecraft, *Space Sci. Rev.*, *91*, 319–359.
- Reinisch, B. W., X. Huang, P. Song, G. S. Sales, S. F. Fung, J. L. Green, D. L. Gallagher, and V. M. Vasyliūnas (2001), Plasma density distribution along the magnetospheric field: RPI observations from IMAGE, *Geophys. Res. Lett.*, *28*, 4521–4524.
- Reinisch, B. W., X. Huang, P. Song, J. L. Green, F. S. Fung, V. M. Vasyliūnas, D. L. Gallagher, and B. R. Sandel (2004), Plasmaspheric mass loss and refilling as a result of a magnetic storm, *J. Geophys. Res.*, *109*, A01202, doi:10.1029/2003JA009948.
- Richmond, A. D. (1995), Ionospheric electrodynamic using magnetic apex coordinates, *J. Geomagn. Geoelectr.*, *47*, 191–212.
- Roger, A. S., R. J. Moffett, and S. Quegan (1992), The role of ion drift in the formation of the ionisation troughs in the mid- and high-latitude ionosphere—A review, *J. Atmos. Terr. Phys.*, *54*, 1–30.
- Sheeley, B. W., M. B. Moldwin, H. K. Rassoul, and R. R. Anderson (2001), An empirical plasmasphere and trough density model: CRESS observations, *J. Geophys. Res.*, *106*, 25,631–25,641.
- Singh, N., and J. L. Horwitz (1992), Plasmasphere refilling: Recent observations and modeling, *J. Geophys. Res.*, *97*, 1049–1079.
- Smith, M. F., and M. Lockwood, *Earth's magnetospheric cusps*, *34*, 233–260, 1996.
- Sojka, J. J., R. W. Schunk, J. F. E. Johnson, J. H. Waite Jr., and C. R. Chappell (1983), Characteristics of thermal and suprathermal ions associated with the dayside plasma trough as measured by the Dynamics Explorer retarding ion mass spectrometer, *J. Geophys. Res.*, *88*, 7895–7911.
- Song, P., C. T. Russell, T. I. Gombosi, and D. L. DeZeeuw (2003), A model of the formation of the low-latitude boundary layer for northward IMF by reconnection: A summary and review, in *Earth's Low-Latitude Boundary Layer*, *Geophys. Monogr. Ser.*, vol. 133, edited by P. T. Newell and T. Onsager, pp. 121–130, AGU, Washington, D.C.
- Tsunoda, R. T., R. C. Livingston, J. F. Vickrey, R. A. Heelis, W. B. Hanson, F. J. Rich, and P. F. Bythrow (1989), Dayside observations of thermal-ion upwelling at 800-km altitude: An ionospheric signature of the cleft ion fountain, *J. Geophys. Res.*, *94*, 15,277–15,290.
- Tsyganenko, N. A. (1995), Modeling the earth's magnetospheric magnetic field confined within a realistic magnetopause, *J. Geophys. Res.*, *100*, 5599–5612.
- Tu, J.-N., J. L. Horwitz, and T. E. Moore (2005), Simulating the cleft ion fountain at Polar perigee altitudes, *J. Atmos. Sol. Terr. Phys.*, *67*, 465–477.

H. U. Frey, Space Sciences Laboratory, University of California, Berkeley, 7 Gauss Way, Berkeley, CA 94720, USA.

J. L. Green, NASA Goddard Space Flight Center, MC 630, Bldg 26, Greenbelt, MD 20771, USA.

X. Huang, B. W. Reinisch, P. Song, and J. Tu, Center for Atmospheric Research, University of Massachusetts-Lowell, 600 Suffolk Street, Lowell, MA 01854, USA. (jiannan\_tu@uml.edu)

P. H. Reiff, Department of Physics and Astronomy, Rice University, 6100 Main Street, Houston, TX 77005, USA.